Received 18 September 2017; revised 14 November 2017; accepted 12 December 2017. Date of publication 27 December 2017; date of current version 8 January 2018. The review of this paper was arranged by Editor E. Sangiorgi.

Digital Object Identifier 10.1109/JEDS.2017.2785618

Scaling and Modeling of High Temperature 4H-SiC p-i-n Photodiodes

SHUOBEN HOU (Student Member, IEEE), PER-ERIK HELLSTRÖM (Member, IEEE), CARL-MIKAEL ZETTERLING (Senior Member, IEEE), AND MIKAEL ÖSTLING (Fellow, IEEE)

School of Information and Communication Technology, KTH Royal Institute of Technology, 16440 Kista, Sweden

CORRESPONDING AUTHOR: S. HOU (e-mail: shuoben@kth.se)

This work was supported by Knut and Alice Wallenberg Foundation as a part of "Working on Venus" Project. Part of this work has been presented at the 75th Device Research Conference 2017.

ABSTRACT 4H-SiC p-i-n photodiodes with various mesa areas (40 000 μm^2, 2500 μm^2, 1600 μm^2, and 400 μm^2) have been fabricated. Both *C–V* and *I–V* characteristics of the photodiodes have been measured at room temperature, 200 °C, 400 °C, and 500 °C. The capacitance and photo current (at 365 nm) of the photodiodes are directly proportional to the area. However, the dark current density increases as the device is scaled down due to the perimeter surface recombination effect. The photo to dark current ratio at the full depletion voltage of the intrinsic layer (−2.7 V) of the photodiode at 500 °C decreases ~7 times as the size of the photodiode scales down 100 times. The static and dynamic behavior of the photodiodes are modeled with SPICE parameters at the four temperatures.

INDEX TERMS 4H-SiC, photodiode, high temperature, scaling.

I. INTRODUCTION

Ultraviolet (UV) photography is important in astronomy, biological and medical analysis. Commercial detectors used in UV photography are Si or GaAs photodiodes in conjunction with UV band pass filters. However, the narrow band gap semiconductors have aging issues in UV detection. The filters also add extra costs and fabrication complexity [1]. Apart from Si and GaAs, wide band gap semiconductors, such as SiC, GaN and ZnO are suitable alternatives for UV photography because only UV light can be collected by them and the materials are naturally transparent to longer wavelength light [1]. Moreover, wide band gap semiconductors have advantages in high temperature and high radiation operations which are required in combustion detection, space exploration, etc [2]. 4H-SiC are more widely investigated for UV detection among the wide band gap semiconductors on account of the low defect density wafers available and more mature processing techniques [3]. We have summarized different types of 4H-SiC based photodiodes that have been published during the past decade (see Table 1) [3]–[18]. Their operational temperatures are promising. However, most of the devices are larger than 10000 μm^2, which are not suitable to be integrated into high resolution UV photography sensors. To produce a full-frame UV-only imaging sensor containing mega-pixels, smaller photodiodes (20 μm by side or smaller) made of 4H-SiC are needed [19]. Moreover, SPICE modeling of the photodiode is also important for integrated circuit (IC) level design of the imaging sensor.

We have reported our 4H-SiC p-i-n photodiode with mesa area of 40000 μm^2 [16]. In this paper three more photodiodes with mesa areas of 2500 μm^2, 1600 μm^2 and 400 μm^2 are fabricated and characterized from room temperature (RT) to 500 °C. The SPICE parameters (marked in capital letters in this paper) of the photodiodes are modeled based on the measurement results. The effective carrier lifetime, photo current and photo to dark current ratio (PDCR) of the photodiodes are also measured or calculated. The relationships between the parameters and temperature and the dimensions of the photodiodes are discussed.

II. DESIGN AND FABRICATION

The photodiodes were fabricated on one 4 inch n-type 4H-SiC substrate with four epitaxial layers (n/p+/n-/n+). The cross-section of each photodiode is shown in Fig. 1(a). The microscope images of the square shaped photodiodes with different n-type mesa areas, namely 200 μm, 50 μm, 40 μm and 20 μm on the side, are shown in Fig. 1(b)-(e).

2168-6734 © 2017 IEEE. Translations and content mining are permitted for academic research only.
Personal use is also permitted, but republication/redistribution requires IEEE permission.
See http://www.ieee.org/publications_standards/publications/rights/index.html for more information.

TABLE 1. 4H-SiC based photodiodes during the past decade.

Reference	Type	Size	Highest Operational Temperature	Typical Responsivity[1]
[3]	PN	1 mm × 1 mm	90 °C	0.11 A/W (280 nm, 0 V)
[4]	APD[2]	120 μm in diameter	175 °C	0.125 A/W (290 nm, 10 V)
[5]	APD	150 μm in diameter	175 °C	0.174 A/W (270 nm, 40 V)
[6]	APD	90-440 μm in diameter	175 °C	0.096 A/W (270 nm, 0 V)
[7]	MSM[3]	500 μm × 158 μm	450 °C	0.0305 A/W (325 nm, 20V)
[8]	Schottky	0.25 mm × 0.5 mm to 1 cm × 1 cm	RT	N/A
[9]	Schottky	0.37 mm^2, 0.43 mm^2	RT	0.16 A/W (256 nm, 20 V)
[10]	PIN	200 μm × 200 μm	RT	0.13 A/W (270 nm, 5 V)
[11]	APD	500 μm × 500 μm and 1 mm × 1 mm	230 °C	0.12 A/W (310 nm)
[12]	APD	100∼240 μm in diameter	RT	0.187 A/W (278 nm, 70 V)
[13]	APD	100 μm in diameter	190 °C	0.093 A/W (280 nm, 20 V)
[14]	APD	100 μm in diameter	RT	0.09 A/W (266 nm, 20 V)
[15]	PN	0.5 mm × 0.5 mm to 2 mm × 2 mm	300 °C	0.175 A/W (320 nm, 0 V)
[16]	PIN	200 μm × 200 μm	550 °C	0.12 A/W (275 nm, 1 V)
[17]	APD	90 μm in diameter	RT	N/A
[18]	Schottky	1.2 mm × 1.2 mm	120 °C	0.093 A/W (270 nm, 15 V)

[1] The bracket includes the corresponding wavelength and reverse bias voltage.
[2] APD: Avalanche Photodiode
[3] MSM: Metal Semiconductor Metal Photodiode

The mesas were etched by reactive ion etching and the contacts were formed by metal deposition and rapid thermal annealing. The cathode (Ni, 950 °C) of each photodiode was a square ring located on the n-type mesa. Two anodes (Ni/Ti/Al, 815 °C) were located on the p-type mesa to allow the symmetrical flow of charge carriers between the cathode and the anodes. The widths of both cathode and anode were 3 μm for the 400 μm^2 photodiode and 6 μm for the larger ones. Besides the anode and cathode, there was an extra electrode connected to the buffer designed to isolate each photodiode by applying a reverse bias. The metal pads for probing were formed by TiW/Al (100 nm/500 nm) metal layers. Since the cathodes with metal layers on top partially blocked the n-type mesas, the actual light detection areas of the photodiodes were 33996 μm^2, 1432 μm^2, 824 μm^2 and 218 μm^2 respectively.

III. MEASUREMENT SETUP

The dynamic, static and optical behavior of the photodiodes were tested by C-V (at 1 MHz) and I-V measurements with a probe station and a parameter analyzer (Keithley 4200 SCS). Each source-measure unit (SMU) in the measurement setup is connected to a preamplifier (4200-PA) to reduce the noise. The measurement limit of the current is 10 fA. The devices were placed on a temperature controlled hot chuck and they were measured at RT, 200 °C, 400 °C and 500 °C. Each cable connected between the probe and the SMU has a heat resistant cladding to protect from high temperatures. To measure the optical response of the photodiodes, a UV LED was used as the illumination source. The LED (P8D1, Seoul Semiconductors) has an emission peak at 365 nm (corresponding to the photon energy of 3.4 eV), FWHM of 18 nm and optical power density of ∼0.8 mW/cm^2 [20].

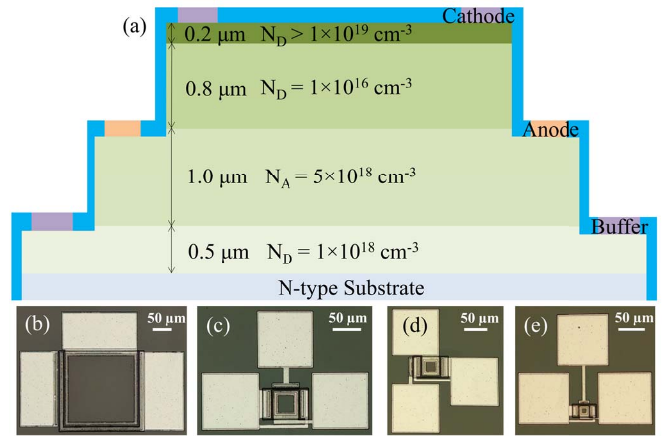

FIGURE 1. (a) Cross-section of the photodiodes with thickness and doping profiles. Microscope images of the photodiodes with top mesa areas of (b) 40000 μm^2, (c) 2500 μm^2, (d) 1600 μm^2 and (e) 400 μm^2.

IV. RESULTS AND DISCUSSIONS

A. C-V CHARACTERISTICS OF THE PHOTODIODES

The C-V curves at forward bias of the 40000 μm^2 photodiode at different temperatures are shown in Fig. 2 (a). The peak capacitance voltage of the C-V curve decreases at higher temperatures due to the built-in potential (VJ) decrease. The reference built-in potential of the diodes can be calculated with Goldberg *et al.*'s empirical model of 4H-SiC [21], which considers the temperature dependent band gap and effective densities of conduction and valence band states. The calculated built-in potential reference (dash line) and the peak capacitance voltage (red symbol) of the diode are plotted in Fig. 2 (b). The peak capacitance voltage follows the same temperature trend as the reference but is ∼0.4 V smaller at each temperature.

Fig. 3 (a) shows the zero bias junction capacitance (CJ0) of the photodiode as a function of temperature. CJ0 increases slightly at higher temperatures. The reason for this is probably because of the increase of effective charge density in the space charge region or deep level defects trapping the carriers [18]. Fig. 3 (b) shows CJ0 as a function of mesa area at 500 °C. CJ0 is directly proportional to the mesa area of the device as expected.

Fig. 4 (symbols) shows the measured C-V curves of the 40000 μm^2 photodiode from reverse bias (-5 V) to small forward bias (1 V). In this bias region, the depletion capacitance of the diode dominates over the diffusion capacitance and the C-V curves can be modeled (see lines in Fig. 4) by Eq.(1) (SPICE model)

$$C = CJ0/(1 - V/(FC \cdot VJ))^M \quad (1)$$

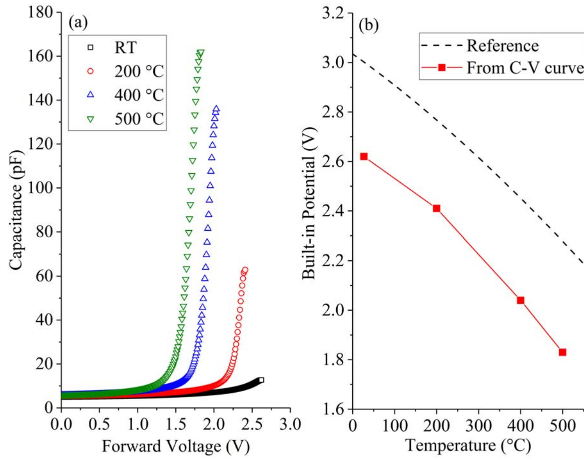

FIGURE 2. **(a) The C-V curves at forward bias of the 40000 μm^2 photodiode at RT, 200 °C, 400 °C and 500 °C. (b) Built-in potential reference [21] (black dash) and peak capacitance voltage (red symbol) of the photodiode as a function of temperature.**

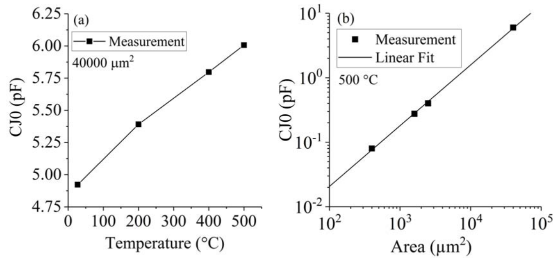

FIGURE 3. **(a) The zero bias junction capacitance (CJ0) of the photodiode increases slightly at higher temperatures. (b) CJ0 of the photodiode is directly proportional to the mesa area.**

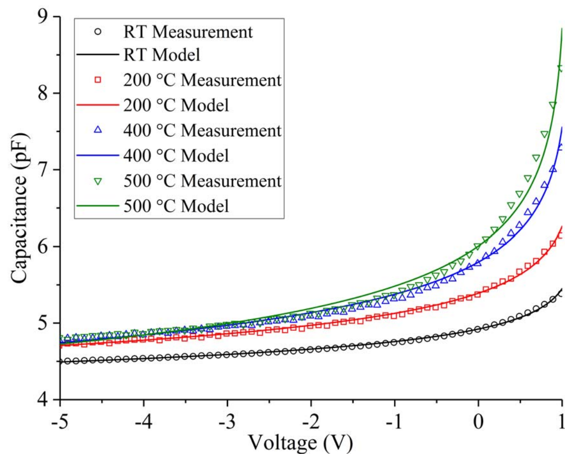

FIGURE 4. **Measured (symbols) and modeled (lines) depletion capacitance of the 40000 μm^2 photodiode at RT, 200 °C, 400 °C and 500 °C.**

where M is the junction grading coefficient, FC is the fraction of the built-in potential, VJ is chosen as the peak capacitance voltage in Fig. 2 (b) and CJ0 is taken from Fig. 3.

With the same equation and measurement method the parameters of the dynamic SPICE model (VJ, CJ0, FC and M) of the four photodiodes at the four temperatures are all modeled and summarized at the end of the discussion.

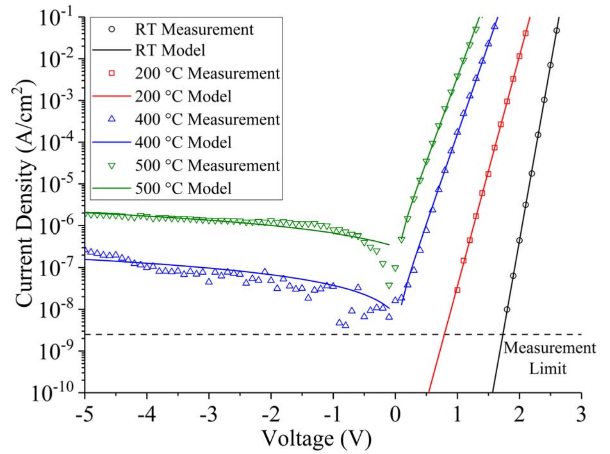

FIGURE 5. **Measured (symbols) and modeled (lines) dark current density of the 400 μm^2 photodiode at RT, 200 °C, 400 °C and 500 °C.**

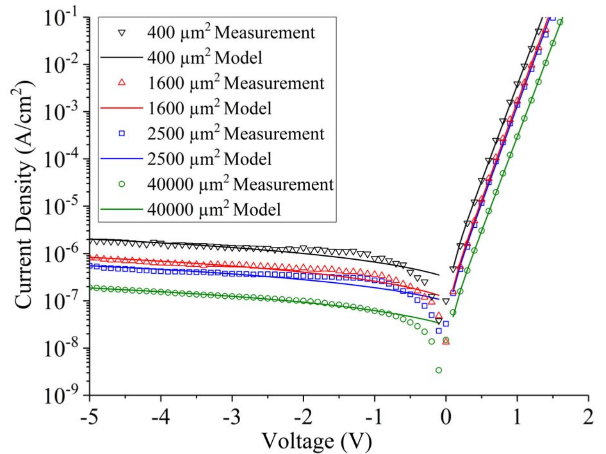

FIGURE 6. **Measured (symbols) and modeled (lines) dark current density of the photodiodes with various mesa areas at 500 °C.**

B. I-V CHARACTERISTICS OF THE PHOTODIODES

Each measured current value from the I-V measurement is firstly divided by the area of the photodiode to get the current density to show the area dependency. The J-V curves of the 400 μm^2 photodiode at different temperatures and without any illumination are shown in Fig. 5 (symbols). The reverse biased dark current at temperatures below 400 °C cannot be accurately measured since it is below the measurement limit (10 fA) of the parameter analyzer. The J-V curves of the photodiodes with various mesa areas at 500 °C are shown in Fig. 6 (symbols).

The forward current of the photodiode has an exponential relationship to the forward voltage as described in Eq.(2) (SPICE model)

$$J = JS\left(exp\left(\frac{qV}{NkT}\right) - 1\right) \tag{2}$$

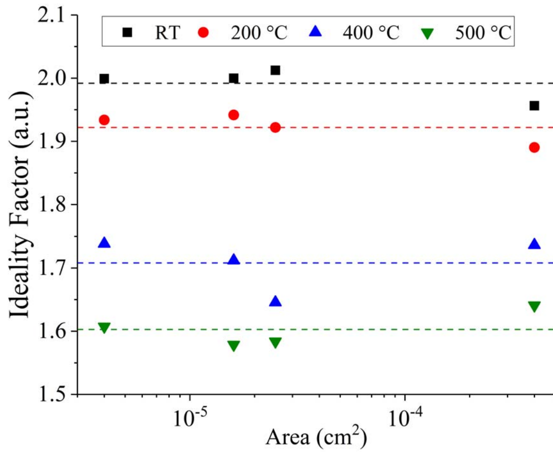

FIGURE 7. Ideality factor of the photodiode extracted from the J-V curves at different temperatures. The dash lines are the average values of the ideality factor at different temperatures.

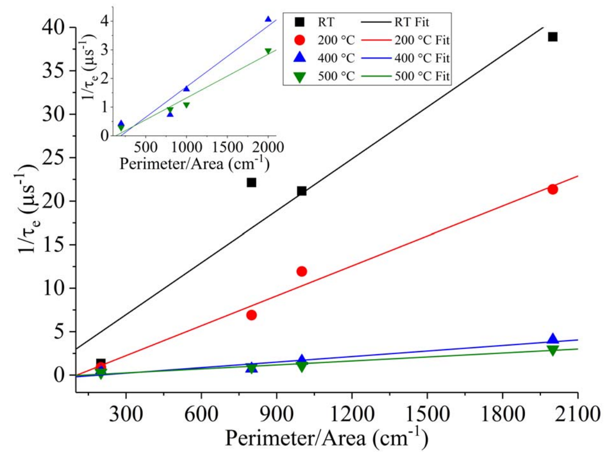

FIGURE 9. Inverse of the effective carrier lifetime (τ_e) as a function of the device perimeter-to-area ratio at different temperatures.

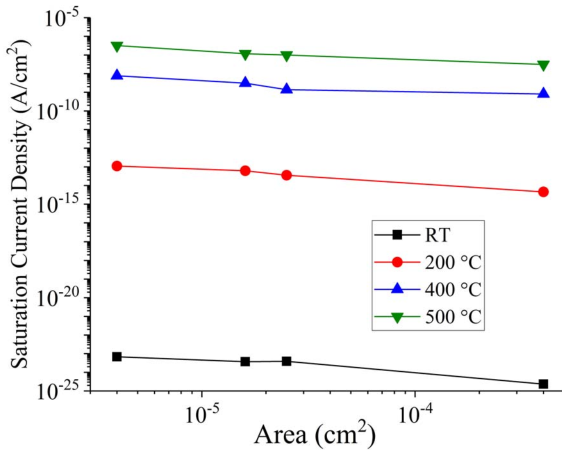

FIGURE 8. Saturation current density of the photodiode extracted from the J-V curves at different temperatures.

where JS is the saturation current density, N is the ideality factor (emission coefficient in SPICE), T is the absolute temperature.

The ideality factor and saturation current density of the photodiodes can be extracted by fitting the measured J-V curves at the forward bias region to Eq.(2). The ideality factor of the photodiode, as shown in Fig. 7, is area independent. Its value is 1.99 (sd. 2.45%, sd. is standard deviation), 1.92 (sd. 2.26%), 1.71 (sd. 4.34%) and 1.60 (sd. 2.84%) at RT, 200 °C, 400 °C and 500 °C respectively. It decreases as the temperature increases because the diffusion current in the neutral region dominates over the recombination current in the depletion region at higher temperatures [22]. The saturation current density of the photodiode at different temperatures is shown in Fig. 8. It increases as the temperature is elevated and it is smaller for larger devices at each temperature, which agrees with the measurement result of dark current in Fig. 6.

The dark current density (or saturation current density) is smaller for larger devices because of the perimeter surface recombination effect [23]. The saturation current density is the sum of diffusion current and generation current [22]

$$JS = q\sqrt{\frac{D_p}{\tau_p}}\frac{n_i^2}{N_D} + \frac{qn_iW}{\tau_e} \tag{3}$$

where D_p is the diffusion coefficient, τ_p is the minority carrier lifetime, n_i is the intrinsic carrier concentration, N_D is the donor concentration, W is the depletion depth (~ 0.8 μm at −2.7 V), τ_e is the effective carrier lifetime. The generation current dominates the saturation current in the diode because n_i of 4H-SiC is low even at 500 °C (~10^{10} cm^{-3}) and the diffusion current component in Eq.(3) can be ignored. Therefore, τ_e can be calculated by substituting the extracted saturation current densities into Eq.(3). The inverse of τ_e as a function of the perimeter to area ratio (PAR) of the photodiode at different temperatures are plotted in Fig. 9. The inset graph is Fig. 9 with a smaller y-axis scale. The inverse of τ_e has a linear relationship to the PAR, which is in accordance to former studies [23]. τ_e decreases as the PAR increases because perimeter surface recombination dominates over the bulk recombination.

The dark current density of the diode at each temperature increases at higher reverse bias because the depletion width increases (see Fig. 5 and Fig. 6). This can be modeled by adding a parallel conductance (GMIN) to the diode, which can be specified in the .OPTIONS statement of SPICE.

The SPICE modeled J-V curves of the photodiodes are plotted in Fig. 5 (line) and Fig. 6 (line) together with the measurement data. The parameters of the static SPICE model (IS, N, GMIN) of the four photodiodes at different temperatures are summarized at the end of the discussion.

The 40000 μm^2 photodiode has optical responsivity from 220 nm to 380 nm (from near to middle UV range) as presented in our former report [16]. To show the relationship between photo current and area the same I-V measurements

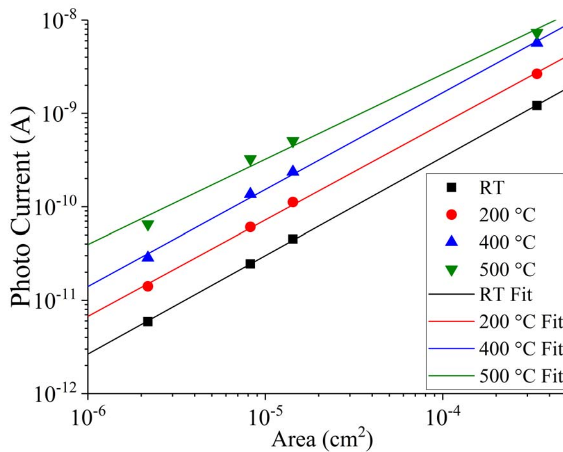

FIGURE 10. Photo current of the photodiodes as a function of the light detection area at different temperatures under the illumination of 365 nm UV light.

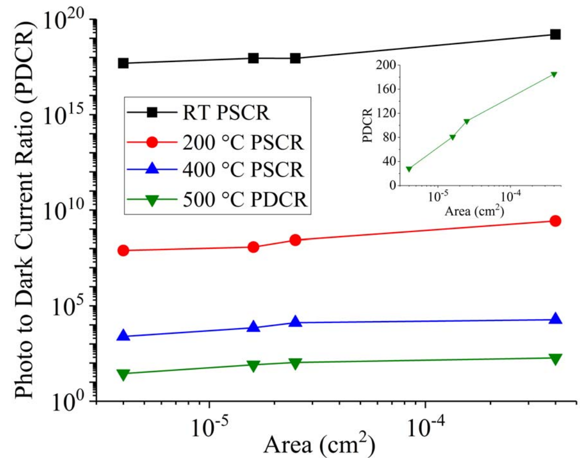

FIGURE 11. PDCR of the photodiodes at -2.7 V (full depletion voltage of the intrinsic layer) at different temperatures.

as above were repeated on the photodiodes with only 365 nm UV illumination. The photo currents of the photodiodes at the reverse bias of 2.7 V (full depletion voltage of the intrinsic layer) are plotted in Fig. 10. At each temperature, the photo current is directly proportional to the detection area, which agrees with the photo current equation of a p-i-n photodiode in [22]. For each photodiode, the photo current increases as the temperature is elevated because band gap narrowing and carrier lifetime increase (see Fig. 9). The band gap narrowing increases the absorption of photons at 365 nm and the increased carrier lifetime reduces the recombination of generated electron-hole pairs, thus inducing an increase of the photo current.

As described above, the dark current density of the photodiode increases as the mesa area becomes smaller, but the photo current density remains constant. Therefore, the PDCR of the photodiode at each temperature decreases as the photodiode is scaled down, as shown in Fig. 11. Note that the photo to saturation current ratios (PSCR) are calculated instead of PDCR at temperature below 400 °C. The inset graph in Fig. 11 is the linear-linear plot of the PDCRs from the measurement results at 500 °C. When the temperature is below 400 °C, the decrease of PDCR due to device scaling can be ignored since the PDCRs are larger than 3 orders of magnitude. However, this phenomenon significantly affects the scaled photodiodes at higher temperatures or under lower level illuminations. At 500 °C, the PDCR of the photodiode decreases ~7 times (from 185 to 28) as the size is scaled down 100 times, which means the smaller photodiode degrades ~7 times in low light detection.

C. SPICE PARAMETERS OF THE PHOTODIODES

Based on the measurement results and modeling equations (Eq.(1) and Eq.(2)) mentioned above, the SPICE parameters of the photodiodes at RT, 200 °C, 400 °C and 500 °C are summarized in Table 2, Table 3, Table 4 and Table 5 respectively. The saturation current (IS) is listed in the tables

TABLE 2. SPICE model of the photodiodes at RT.

Size (μm^2)	IS (A)	N	GMIN (Ω^{-1})	CJ0 (pF)	VJ (V)	FC	M
40000	9.36E-29	1.96	NA	4.92	2.62	0.46	5.54E-2
2500	9.67E-29	2.01	NA	0.32	2.74	0.46	7.33E-2
1600	5.92E-29	2.00	NA	0.22	2.62	0.48	6.30E-2
400	2.72E-29	2.00	NA	9.8E-3	2.58	NA	NA

TABLE 3. SPICE model of the photodiodes at 200 °C.

Size (μm^2)	IS (A)	N	GMIN (Ω^{-1})	CJ0 (pF)	VJ (V)	FC	M
40000	1.82E-18	1.89	NA	5.39	2.41	0.49	8.23E-2
2500	8.92E-19	1.92	NA	0.35	2.5	0.5	9.65E-2
1600	9.87E-19	1.94	NA	0.25	2.49	0.48	8.07E-2
400	4.41E-19	1.93	NA	6.4E-2	2.51	0.52	9.60E-2

TABLE 4. SPICE model of the photodiodes at 400 °C.

Size (μm^2)	IS (A)	N	GMIN (Ω^{-1})	CJ0 (pF)	VJ (V)	FC	M
40000	3.23E-13	1.74	8.53E-10	5.80	2.04	0.55	1.18E-1
2500	3.46E-14	1.65	1.89E-8	0.39	2.15	0.5	1.17E-1
1600	4.90E-14	1.71	7.30E-9	0.28	2.16	0.5	1.07E-1
400	3.07E-14	1.74	2.99E-8	8.4E-2	2.18	0.51	9.77E-2

TABLE 5. SPICE model of the photodiodes at 500 °C.

Size (μm^2)	IS (A)	N	GMIN (Ω^{-1})	CJ0 (pF)	VJ (V)	FC	M
40000	1.24E-11	1.64	3.13E-8	6.01	1.83	0.59	1.38E-1
2500	2.48E-12	1.58	9.09E-8	0.40	1.97	0.53	1.48E-1
1600	1.88E-12	1.58	1.43E-7	0.28	1.97	0.52	1.35E-1
400	1.28E-12	1.61	3.43E-7	8.0E-2	2.02	0.51	1.28E-1

instead of saturation current density. The junction grading coefficient (M) in the model is smaller than the common values (between 0.33 and 0.5). It is probably due to the non-uniform doping concentration of the epitaxial layers, especially the intrinsic layer. The values of FC and M are not available for the 400 μm^2 photodiode at RT because the measurement is below the lower limit of the parameter analyzer and modeling is not possible. The value of GMIN is not available for all the photodiodes at RT and 200 °C for the same reason.

In SPICE IC simulations, the photodiode can be regarded as the equivalent circuit shown in Fig. 12 since there is

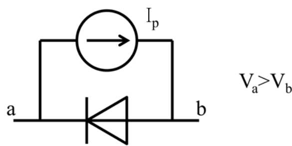

FIGURE 12. The equivalent circuit of a photodiode in SPICE.

no photodiode component in SPICE. The value of the DC current source equals the photo current (I_p) of the photodiode at reverse bias, which should be adjusted according to measurement values.

V. CONCLUSION

Four 4H-SiC based p-i-n photodiodes with mesa areas of 40000 μm^2, 2500 μm^2, 1600 μm^2 and 400 μm^2 were fabricated. Each photodiode was characterized from RT to 500 °C. At each temperature, the capacitance and photo current are directly proportional to the mesa area of the photodiode and the ideality factor remains constant. However, the saturation current density increases as the photodiode is scaled down. This scaling effect is because the perimeter surface recombination dominates on smaller devices, which is shown by the relationship between the effective carrier lifetime and the perimeter to area ratio. The scaled photodiodes with smaller areas have degradations in PDCR but they still show stable operations even at 500 °C. The 400 μm^2 photodiode is a promising candidate for high resolution UV photography sensors for high temperature applications.

REFERENCES

[1] E. Monroy, F. Omnès, and F. Calle, "Wide-bandgap semiconductor ultraviolet photodetectors," *Semicond. Sci. Technol.*, vol. 18, no. 4, pp. R33–R51, Mar. 2003.

[2] C.-M. Zetterling, L. Lanni, R. Ghandi, B. G. Malm, and M. Östling, "Future high temperature applications for SiC integrated circuits," *Physica Status Solidi (c)*, vol. 9, no. 7, pp. 1647–1650, Jul. 2012.

[3] A. Sciuto, M. Mazzillo, S. D. Franco, F. Roccaforte, and G. D'Arrigo, "Visible blind 4H-SiC P^+-N UV photodiode obtained by Al implantation," *IEEE Photon. J.*, vol. 7, no. 3, pp. 1–6, Jun. 2015.

[4] D. Zhou *et al.*, "High-temperature single photon detection performance of 4H-SiC avalanche photodiodes," *IEEE Photon. Technol. Lett.*, vol. 26, no. 11, pp. 1136–1138, Jun. 1, 2014.

[5] X. Cai *et al.*, "4H-SiC SACM avalanche photodiode with low breakdown voltage and high UV detection efficiency," *IEEE Photon. J.*, vol. 8, no. 5, pp. 1–7, Oct. 2016.

[6] S. Yang *et al.*, "4H-SiC p-i-n ultraviolet avalanche photodiodes obtained by Al implantation," *IEEE Photon. Technol. Lett.*, vol. 28, no. 11, pp. 1185–1188, Jun. 1, 2016.

[7] W.-C. Lien *et al.*, "4H–SiC metal–semiconductor–metal ultraviolet photodetectors in operation of 450 °C," *IEEE Electron Device Lett.*, vol. 33, no. 11, pp. 1586–1588, Nov. 2012.

[8] F. Yan *et al.*, "4H-SiC UV photo detectors with large area and very high specific detectivity," *IEEE J. Quantum Electron.*, vol. 40, no. 9, pp. 1315–1320, Sep. 2004.

[9] A. Sciuto, F. Roccaforte, S. D. Franco, V. Raineri, and G. Bonanno, "High responsivity 4H-SiC Schottky UV photodiodes based on the pinch-off surface effect," *Appl. Phys. Lett.*, vol. 89, no. 8, Aug. 2006, Art. no. 081111.

[10] X. Chen, H. Zhu, J. Cai, and Z. Wu, "High-performance 4H-SiC-based ultraviolet p-i-n photodetector," *J. Appl. Phys.*, vol. 102, no. 2, Apr. 2007, Art. no. 024505.

[11] H.-Y. Cha, S. Soloviev, S. Zelakiewicz, P. Waldrab, and P. M. Sandvik, "Temperature dependent characteristics of nonreach-through 4H-SiC separate absorption and multiplication APDs for UV detection," *IEEE Sensors J.*, vol. 8, no. 3, pp. 233–237, Mar. 2008.

[12] X. Guo *et al.*, "Demonstration of ultraviolet separate absorption and multiplication 4H-SiC avalanche photodiodes," *IEEE Photon. Technol. Lett.*, vol. 18, no. 1, pp. 136–138, Jan. 2006.

[13] X. Bai, X. Guo, D. C. Mcintosh, H.-D. Liu, and J. C. Campbell, "High detection sensitivity of ultraviolet 4H-SiC avalanche photodiodes," *IEEE J. Quantum Electron.*, vol. 43, no. 12, pp. 1159–1162, Dec. 2007.

[14] K. Li, H.-D. Liu, Q. Zhou, D. McIntosh, and J. C. Campbell, "SiC avalanche photodiode array with microlenses," *Opt. Exp.*, vol. 18, no. 11, pp. 11713–11719, May 2010.

[15] N. Watanabe, T. Kimoto, and J. Suda, "4H-SiC pn photodiodes with temperature-independent photoresponse up to 300 °C," *Appl. Phys. Exp.*, vol. 5, no. 9, Aug. 2012, Art. no. 094101.

[16] S. Hou, P.-E. Hellström, C.-M. Zetterling, and M. Östling, "550 °C 4H-SiC p-i-n photodiode array with two-layer metallization," *IEEE Electron Device Lett.*, vol. 37, no. 12, pp. 1594–1596, Dec. 2016.

[17] R. A. Berechman, M. Skowronski, S. Soloviev, and P. Sandvik, "Electrical characterization of 4H-SiC avalanche photodiodes containing threading edge and screw dislocations," *J. Appl. Phys.*, vol. 107, no. 11, Jun. 2010, Art. no. 114504.

[18] G. Lioliou, M. C. Mazzillo, A. Sciuto, and A. M. Barnett, "Electrical and ultraviolet characterization of 4H-SiC Schottky photodiodes," *Opt. Exp.*, vol. 23, no. 17, pp. 21657–21670, Aug. 2015.

[19] S. Hou, P.-E. Hellström, C.-M. Zetterling, and M. Östling, "Scaling of 4H-SiC p-i-n photodiodes for high temperature applications," in *Proc. 75th Annu. Device Res. Conf. (DRC)*, South Bend, IN, USA, Jun. 2017, pp. 1–2.

[20] S. Hou, P. E. Hellström, C. M. Zetterling, and M. Östling, "4H-SiC PIN diode as high temperature multifunction sensor," in *Silicon Carbide and Related Materials 2016* (Materials Science Forum), vol. 897. Zürich, Switzerland: Trans Tech, May 2017, pp. 630–633.

[21] Y. Goldberg, M. E. Levinshtein, and S. L. Rumyantsev, *Properties of Advanced Semiconductor Materials: GaN, AIN, InN, BN, SiC, SiGe*, M. E. Levinshtein, S. L. Rumyantsev, and M. S. Shur, Eds. New York, NY, USA: Wiley, 2001.

[22] S. M. Sze and K. K. Ng, Eds., *Physics of Semiconductor Devices*. Hoboken, NJ, USA: Wiley, 2006.

[23] P. G. Neudeck and C. Fazi, "Nanosecond risetime pulse characterization of SiC p^+n junction diode breakdown and switching properties," *Mater. Sci. Forum*, vols. 264–268, pp. 1037–1040, Feb. 1998.

SHUOBEN HOU received the B.Eng. degree in opto-electronics from the Harbin Institute of Technology, China, in 2011, the M.Sc. degree in photonics from the European (Erasmus Mundus) Master of Science in Photonics program, organized jointly by Ghent Univeristy and VUB, Belgium and the University of St. Andrews, U.K., in 2013. He is currently pursuing the Ph.D. degree with the KTH Royal Institute of Technology, Sweden. His current research interests include SiC-based opto-electronic devices and integrated circuits for high temperature applications.

PER-ERIK (HELLBERG) HELLSTRÖM was born in Stockholm, Sweden, in 1970. He received the M.Sc. and Ph.D. degrees in electrical engineering from the KTH Royal Institute of Technology, Stockholm, in 1995 and 2000, respectively. His Ph.D. thesis dealt with polycrystalline $Si_{1-x}Ge_x$ as gate material for CMOS technology. Since 2000, he has been a Research Associate with the KTH School of Information and Communication Technology, where he was appointed as a Docent in 2006. He has co-authored over 100 papers in refereed journals and conference proceedings. His current research interests include semiconductor process technology, advanced nano-scaled MOSFETs, monolithic 3-D integration technology and devices for sensing applications.

CARL-MIKAEL ZETTERLING (S'91–M'97–SM'01) received the M.Sc.E.E. and Ph.D. degrees from the KTH Royal Institute of Technology, Stockholm, Sweden, in 1991 and 1997, respectively, where he has been a Professor of solid-state electronics since 2005. His field of research is process technology and device design for high-voltage devices and high-temperature analog and digital integrated circuits in SiC.

MIKAEL ÖSTLING (M'85–SM'97–F'04) received the M.Sc. and Ph.D. degrees from Uppsala University, Sweden. He is currently a Professor of solid-state electronics and a Deputy President with the KTH Royal Institute of Technology, Sweden. Since 2016, he has been the Editor-In-Chief of the IEEE JOURNAL OF THE ELECTRON DEVICES SOCIETY. His research interests are Si/SiGe devices and process technology for very high frequency, and also device technology for wide bandgap semiconductors with special emphasis on SiC for high power and high temperature applications.